Strong Room-Temperature Ferroelectricity in Strained SrTiO₃ Homoepitaxial Film

Tianyu Li, Dengshi Qing, Hui Liu, Shengdong Sun, Hao Li, Shuxian Hu, Shi Liu, Xianran Xing, and Jun Chen*

Although the discovery of exceptional ferroelectricity in paraelectrics offers great opportunities to enrich the diversity of the ferroelectric family and promote the development of novel functionalities, transformation of paraelectric phases into ferroelectric phases remains challenging. Herein, a method is presented for driving paraelectrics into ferroelectric states via the introduction of M/O-deficient (M for metal) perovskite nanoregions. Using this method, strong ferroelectricity, equivalent to that of classic ferroelectrics, is achieved in a prototype paraelectric strontium titanate ($SrTiO_3$) homoepitaxial film embedded with Ti/O-deficient perovskite nanoregions. It is shown that these unique nanoregions impose large out-of-plane tensile strain and electron-doping effects on the matrix to form a tetragonal structure (tetragonality = 1.038), driving the off-center movements of Ti and Sr atoms. This leads to a significant room-temperature ferroelectric polarization (maximum polarization = 41.6 µC cm⁻² and spontaneous polarization = 25.2 µC cm⁻² at 1.60 MV cm⁻¹) with a high thermal stability ($T_{stable} \approx 1098$ K). The proposed approach can be applied to various paraelectrics for creating ferroelectricity and generating emergent physical properties, opening the door to a new realm of materials design.

1. Introduction

Ferroelectricity is an intriguing property of functional materials, enabling broad applications of these materials in information storage, energy utilization, and electromechanical transformation.[1] Among the well-developed ferroelectrics, perovskite oxides such as $PbTiO_3$ and $BaTiO_3$ possess outstanding properties, because a perovskite structure can provide an essential spatiotemporal dimension for the emergence of spontaneous polarization (P_s) and its evolution under external electric fields.[2] Therefore, the perovskite structure can be a flexible platform for tuning and optimizing ferroelectric properties. To enhance ferroelectric polarization, numerous intriguing strategies have been proposed, including chemical substitution[3] and introduction of epitaxial biaxial strain and interphase strain.[4] Notably, most related studies are mainly focused on optimizing the ferroelectric performance of existing ferroelectrics.[5] Interestingly, although emergent ferroelectricity has been previously reported in some nonferroelectric systems, there still exist a large number of paraelectrics that can potentially be transformed into ferroelectrics by a generally applicable method.[6] In this regard, developing a methodology for converting paraelectrics into ferroelectrics would considerably enrich the diversity of the ferroelectric family and provide more opportunities for the application in modern electronic devices.

As a paraelectric perovskite prototype, $SrTiO_3$ was first synthesized in the 1920s.[7] It has been widely used in electronic devices for more than half a century owing to its excellent dielectric properties, high thermal stability, and facile synthesis. Although the thermal disorder of the atoms reduces with a decrease in temperature, the alignment of electric dipoles is still hindered in $SrTiO_3$ due to quantum fluctuation under an absolute zero-point vibration.[8] Considerable efforts have been devoted to the exploration of ferroelectricity in $SrTiO_3$ via various methods such as isotope substitution[9] and utilization of interfacial strain,[10] intrinsic defects,[11] and freestanding membranes.[12] However, to date, only weak ferroelectricity has been achieved in $SrTiO_3$, which hinders the promising applications.

Herein, strong room-temperature ferroelectricity was realized in the $SrTiO_3$ homoepitaxial films by the introduction of

T. Y. Li, S. D. Sun, H. Li, Prof. J. Chen
Beijing Advanced Innovation Center for Materials Genome Engineering
Department of Physical Chemistry
University of Science and Technology Beijing
Beijing 100083, China
E-mail: junchen@ustb.edu.cn
Dr. D. Qing, Dr. H. Liu, Prof. S. X. Hu, Prof. J. Chen
School of Mathematics and Physics
University of Science and Technology Beijing
Beijing 100083, China
Prof. S. Liu
School of Science
Key Laboratory of Quantum Materials of Zhejiang Provinces
Westlake Institute for Advanced Study
Westlake University
Hangzhou, Zhejiang 310024, China
Prof. X. R. Xing
Beijing Advanced Innovation Center for Materials Genome Engineering
Institute of Solid State Chemistry
University of Science and Technology Beijing
Beijing 100083, China

**ADVANCED
SCIENCE NEWS**
www.advancedsciencenews.com

**ADVANCED
MATERIALS**
www.advmat.de

Ti/O-deficient perovskite nanoregions. The $SrTiO_3$ homoepitaxial film embedded with Ti/O-deficient perovskite nanoregions demonstrated a maximum polarization (P_{max}) of 41.6 µC cm^{-2} with an increased tetragonality ($c/a = 1.038$) and an extremely high thermal stability (T_{stable}) of up to 1098 K. Its strong macroscopic ferroelectric properties were confirmed by ferroelectric hysteresis measurements and piezoelectric force microscopy (PFM). A combination of atomic-scale scanning transmission electron microscopy (STEM), X-ray absorption spectroscopy (XAS), and Raman spectroscopy investigations systematically revealed that tensile strain was imposed on the surrounding lattices by Ti and O vacancies in the nanoregions. This caused a cubic–tetragonal structure transition and strengthened the Ti 3d–O 2p orbital hybridization along with polar vibration modes, resulting in polar displacements of Ti and Sr atoms in the film. Density functional theory (DFT) calculations further elucidated that this ferroelectric order featuring a typical double-well Landau energy profile was intrinsically stabilized by the electron-doping effect in the Ti/O-deficient unit cell. The present study suggests that accurate control of different constituent elements in paraelectrics can be an effective way for discovering new ferroelectric materials or other functional materials.

2. Results and Discussion

In this study, we fabricated the homoepitaxial thin films on (001)-oriented $SrTiO_3$ substrates by pulsed laser deposition, and the $SrO:TiO_2$ molar ratio was optimized to 0.55:0.45 to realize optimal Ti/O-deficient perovskite nanoregions in the thin film. **Figure 1**a shows a typical out-of-plane $\theta/2\theta$ synchrotron-based X-ray diffraction (XRD) pattern of the thin film. Interestingly, although this homojunction was free from the interfacial strain between the thin film and the substrate, the (00*l*) peaks originating from the *c*-oriented epitaxial $SrTiO_3$ film showed a dramatic shift as compared to those arising from the $SrTiO_3$ substrate. Reciprocal space mapping near the (103) spot verified that the in-plane lattice of the thin film appropriately matched that of the substrate and the expanded out-of-plane lattice (Figure 1b). This manifested a significant increase in the lattice parameter *c* from 3.903 Å in the substrate to 4.050 Å in the thin film, corresponding to a large tensile strain of 3.8% inside the thin film. A subsequent phi-scan around the (103) plane indicated a fourfold in-plane symmetry of the thin films and a cube-on-cube epitaxial relationship (Figure 1c). Note that the $SrTiO_3$ homoepitaxial thin film exhibited an interesting tetragonal structure with $c/a = 1.038$, which was even greater than that of
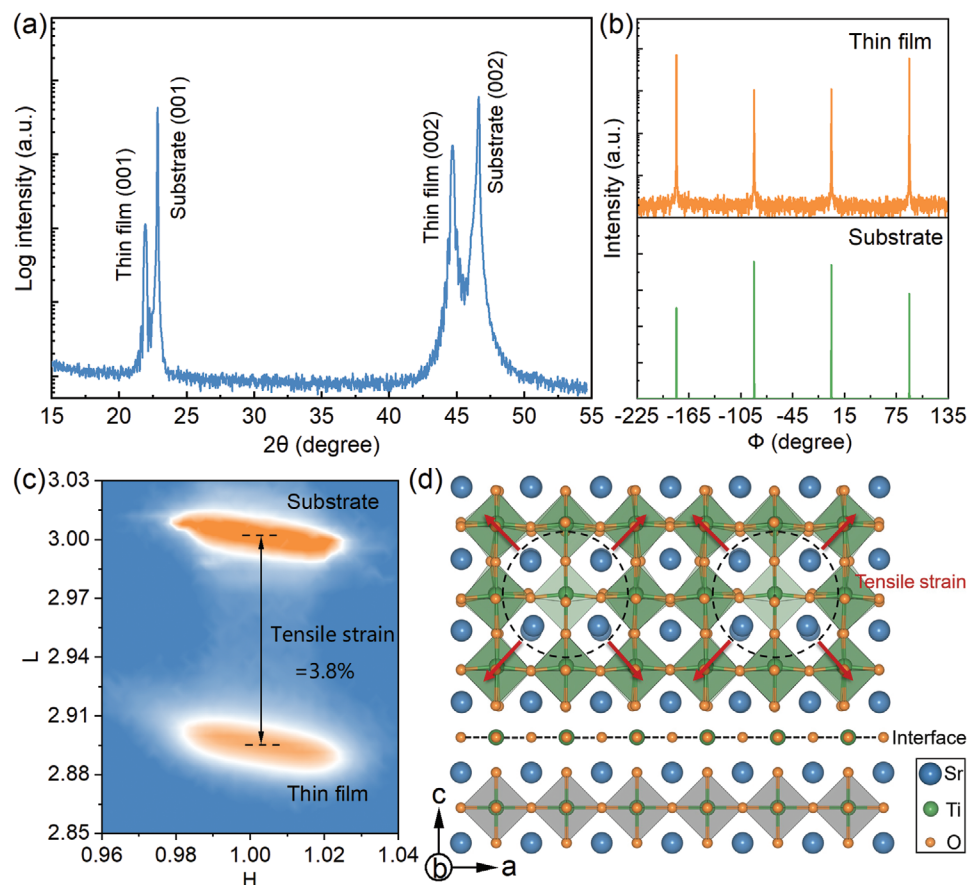
Figure 1. Structural determination of the strained tetragonal $SrTiO_3$ homoepitaxial thin film. a) Synchrotron-based out-of-plane $\theta/2\theta$ XRD pattern. b) Phi scans of the (103) plane of the thin film and substrate. c) Reciprocal space mapping near the (103) spot of the substrate, where H and L represent the (h00) and (00l) Miller indices, respectively. d) Schematic of the calculated structure of $SrTiO_3$ system along the *b*-axis, where Ti/O-deficient unit cells are marked by the dashed circles.

**ADVANCED
SCIENCE NEWS**

www.advancedsciencenews.com

**ADVANCED
MATERIALS**

www.advmat.de
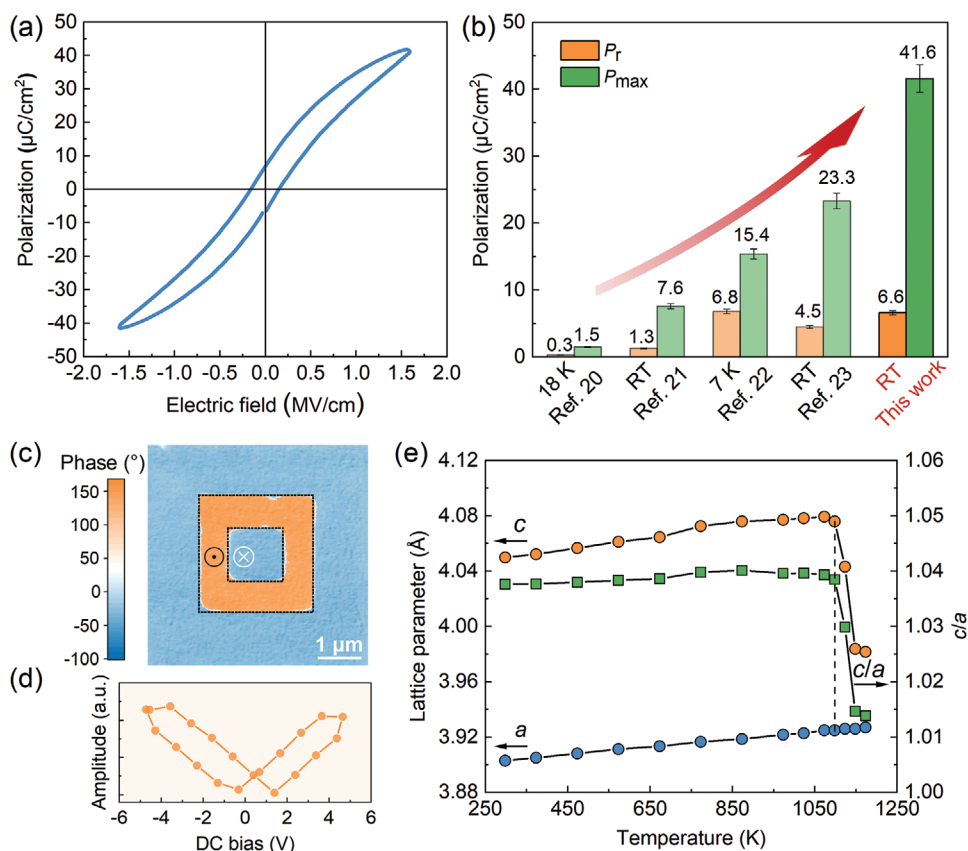
Figure 2. Ferroelectric properties of the strained tetragonal SrTiO$_3$ homoepitaxial thin film. a) Polarization–electric field hysteresis loop of the thin film. b) Comparisons of remnant polarization (P_r) and maximum polarization (P_{max}) obtained in the present study with those reported in the previous studies for SrTiO$_3$ films. c) Out-of-plane phase image of the thin film after writing a box-in-box pattern. d) Amplitude hysteresis loop from the local piezoelectric response in the thin film. e) Temperature dependence of lattice parameters and c/a ratios for the thin film and substrate.

BaTiO$_3$ ($c/a = 1.009$) and comparable to that of PbTiO$_3$ ($c/a = 1.064$).[13] For comparison, a normal SrTiO$_3$ film was prepared under the same growth conditions using the target (SrTiO$_3$) with a stoichiometric composition of SrO:TiO$_2$ = 1:1, which clearly did not show any lattice strain (Figure S1, Supporting Information). Therefore, the large c/a can be safely attributed to the changes in the chemical composition of the film, excluding the possibility of formation of byproducts during the growth process.

A ferroelectric state is readily established within the tetragonal structure ($c/a > 1$) in perovskite oxides. As shown in **Figure 2**a and Figure S2 in the Supporting Information, the polarization–electric field (P–E) loop of the SrTiO$_3$ thin film possessed all the characteristics of a typical ferroelectric material. The P_{max} reached as high as 41.6 μC cm^{-2}, and the remnant polarization (P_r) was ≈ 6.6 μC cm^{-2} at room temperature. This P_{max} is almost twice the highest value previously reported for SrTiO$_3$ (Figure 2b), and the P_s (25.2 μC cm^{-2}) extracted from the P–E loop is of the same magnitude as that of prototype ferroelectrics such as BaTiO$_3$ ($P_s \approx 26$ μC cm^{-2}).[14] This large ferroelectric polarization in SrTiO$_3$ is significantly different from the previously reported case, where only weak ferroelectricity was achieved mainly far below room temperature or within very finite regions.[9–12] Furthermore, the possible contributions from the film–substrate interface or the SrTiO$_3$

substrate to this strong ferroelectricity were safely excluded by testing the normal SrTiO$_3$ epitaxial thin film and the substrate, which showed negligible polarization (Figure S3, Supporting Information).

Strong ferroelectricity in the tetragonal SrTiO$_3$ homoepitaxial thin film was further verified by PFM, which allowed us to study its domain structure and its switchable behavior. Surface morphology of the thin film was atomically smooth, as demonstrated by atomic force microscopy (Figure S4, Supporting Information). By applying a bias voltage of ±10 V to the conductive tip, we electrically wrote an out-of-plane box-in-box pattern in a 5 × 5 μm^2 area of the film (Figure S4, Supporting Information). Reversal of phase contrast upon poling indicates that the orientation of the spontaneous polarization in pure ferroelectric domains can be switched under external electric fields (Figure 2c). Moreover, the piezoelectric hysteresis loops as a function of dc voltage provide sufficient evidence of the continuous rotation of electric dipoles and hysteretic behavior in the thin film (Figure 2d; Figure S5, Supporting Information).

For perovskite-type displacive ferroelectrics, enhanced c/a ratio suggests an elevated Curie temperature (T_C).[4b,15] The thermal stability of the strained tetragonal SrTiO$_3$ homoepitaxial thin film was further investigated using temperature-dependent XRD. As shown in Figure 2e, the strained tetragonal phase in the thin film exhibits an unexpectedly enhanced T_{stable}

**ADVANCED
SCIENCE NEWS**

www.advancedsciencenews.com

**ADVANCED
MATERIALS**

www.advmat.de
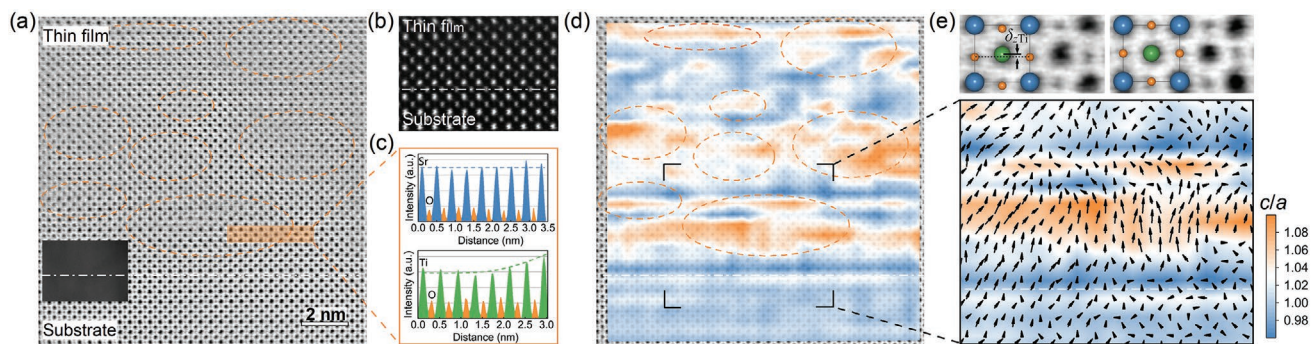
Figure 3. Atomic-scale electron microscopy analysis of the homoepitaxial thin film. a) ABF-STEM image of the thin film along the *b*-axis. Abnormal regions inside the film are marked by dashed circles. The inset shows the cross-sectional homoepitaxial structure at a low magnification. b) HAADF-STEM image of the region near the interface. c) Inverted intensity profiles of Sr–O and Ti–O atomic columns (top and bottom, respectively) from left to right in the orange rectangle in (a). d) c/a contour plots of the unit cells in (a). On the bottom right is a magnified region of the box in (d) superposed with polar vector mapping. The black arrows represent displacement vectors of the off-center Sr and Ti atoms relative to oxygen polyhedral. e) Magnified images of the unit cells acquired from the tetragonal nanoregion (left) and centrosymmetric normal part (right) superposed with the corresponding atomic schematics. Relative displacement of Ti is denoted as $\delta_{z_{Ti}}$.

of 1098 K, which implies that the ferroelectricity of this film can also be maintained at this temperature. The remarkable value of T_{stable} is higher than the T_C of BaTiO$_3$ (403 K) and PbTiO$_3$ (763 K) and comparable to the T_{stable} of supertetragonal PbTiO$_3$ thin films (998 K) and the T_C of BiFeO$_3$ (1109 K).[4d,16] This behavior is attributed to the prominent enhancement effect of the out-of-plane tensile strain on the structural stability of the film. In addition, the sudden reduction in the c/a ratio above T_{stable} is caused by the irreversible collapse of the lattice strain. By combing these results with those of the dielectric temperature spectroscopy, it can be concluded that the ferroelectric-to-paraelectric phase transition of the thin film can even occur above 1098 K.

To reveal the microscopic origins of this tetragonal structure and strong ferroelectricity, atomic-scale microstructure analysis was performed using spherical aberration-corrected STEM. High quality of the thin film was first verified by high-angle annular dark-field (HAADF) imaging (**Figure 3**b; Figure S6, Supporting Information), which manifested an atomic-level sharp interface. As circled in the annular bright-field (ABF) image (Figure 3a), abnormal nanoregions in the range from several to a dozen nanometers were observed and randomly distributed inside the film. To distinguish the structures of the nanoregions and the normal part, intensity profiles of the Ti–O and Sr–O atomic columns in a randomly selected area marked by the orange rectangle in Figure 3a were acquired. Intensities of the Sr–O atomic columns remained almost unchanged from the normal part to the nanoregion, whereas a notable decrease in the intensities of Ti–O column was observed in the nanoregion, as shown by the dashed outlines in Figure 3c. Normalized intensities of Sr and Ti atomic columns and the corresponding standard deviations (SDs) were further calculated from different HAADF images (Table S1, Supporting Information). The average SD of Ti sublattice in the thin film (3.33%) was greater than that of the substrate (1.94%). However, the average SDs of the Sr atomic columns were 1.98% and 1.53% in the thin film and the substrate, respectively. From the atomic-resolution energy-dispersive X-ray spectroscopy (EDXS) results (Figure S7, Supporting Information), no signs of elemental enrichment

were found in the film. This suggested the presence of a Ti/O-deficient state in the nanoregions, which also coincided with the fact that SrO was rich in the target (SrO:TiO$_2$ = 0.55:0.45) used for film deposition. Generally, the Ruddlesden–Popper structure is formed if an excessive amount of SrO is used.[17] In contrast, herein, an excessive amount of SrO tended to grow as a perovskite structure, forming randomly distributed Ti/O-deficient perovskite-type nanoregions having coherent interfaces with the SrTiO$_3$ perovskite-structure matrix in the present thin film.

Tetragonal distortion can drive atoms to deviate from their original positions, causing the emergence of dipole moments. By tracking all the Sr and Ti atomic positions in the area shown in Figure 3a, we quantitatively determined the local tetragonality of the lattice, and the maps of the c/a ratio and polarization vector are presented in Figure 3d. Intriguingly, the Ti/O-deficient perovskite nanoregions featured both an increased c/a ratio and large polarizations of the Sr and Ti atoms, whereas the other part, including the lattices outside the nanoregions and the substrate, possessed a less strained structure and negligible polarizations. Moreover, the distortion behavior of the thin film was further confirmed by different images and was consistent with the strain mapping obtained by a different method of geometric phase analysis (Figures S6 and S8, Supporting Information). Figure 3e shows a comparison between the distinct polar displacements of the Ti atoms ($\delta_{z_{Ti}} \approx 0.20$ Å) in the unit cells of the nanoregion and in the centrosymmetric unit cells of the normal part. The results unambiguously indicate that the Ti/O-deficient perovskite nanoregions can induce cubic-to-tetragonal phase transformation and generate spontaneous polarization by imposing an out-of-plane tensile strain on the surrounding lattice. Thus, it caused the dechanneling effect and the consequently slight blurring of the ABF-STEM image. If the Ti/O-deficient perovskite regions are regarded as an unprecedented Sr-rich second phase at the nanoscale, the present tensile lattice strain can broaden the boundary of the interphase strain.[4d] In addition, these randomly distributed nanoregions with a nonuniform size and polar directions may be responsible for the relaxor-like character of the hysteresis loop (Figure 2a; Figure S2, Supporting Information).[18]

ADVANCED
SCIENCE NEWS
www.advancedsciencenews.com

ADVANCED
MATERIALS
www.advmat.de
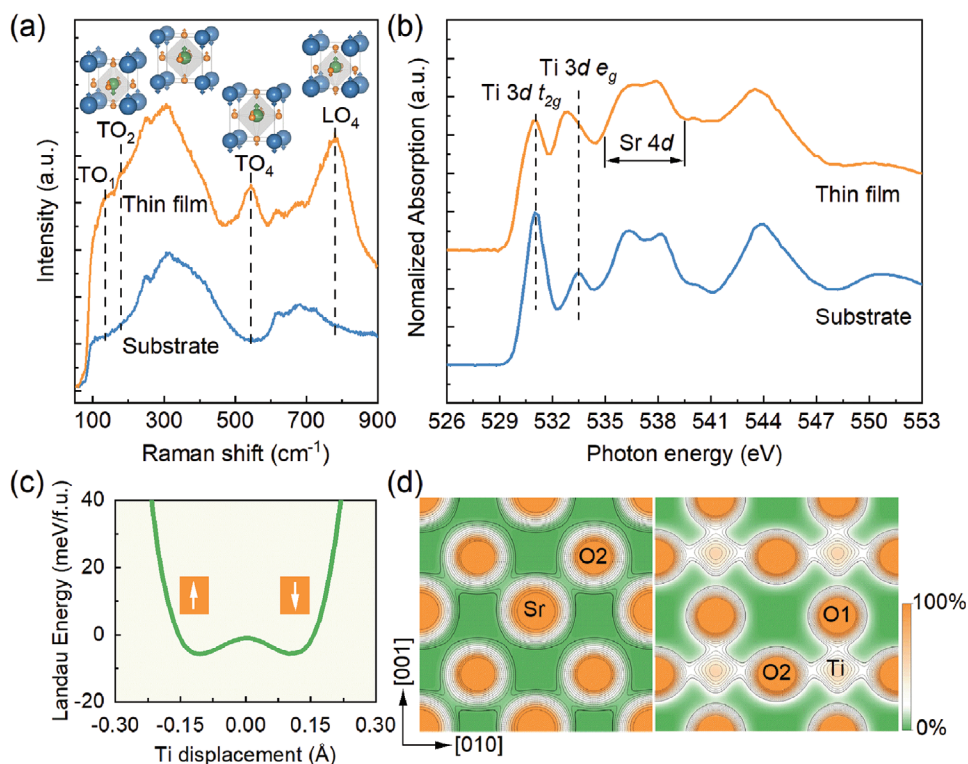
Figure 4. Lattice dynamics and electronic structure analysis. a) Raman spectra of the thin film and substrate. The insets show schematics of the relative atomic vibrations in TO_1, TO_2, TO_4, and LO_4 polar modes. b) O K-edge XAS of the thin film and substrate after normalization to the edge jump. c) Landau energy profile of strained $SrTiO_3$ system. d) Valence-electron density distributions of supercell in the (100) Sr–O plane (left) and (200) Ti–O plane (right). In the color bar, 0% and 100% correspond to 0.01 and 0.25 e $Bohr^{-3}$.

The appearance of strong ferroelectricity in the proposed film can be elucidated by investigating the lattice dynamics and interactions between electron orbitals. If a ferroelectric state occurs with a broken inversion center, the lattice dynamics, specially polar soft modes, in the Raman spectrum substantially change. As shown in **Figure 4**a, the first-order polar peaks (TO_1, TO_2, TO_4, and LO_4), which should be forbidden in the ideal cubic $SrTiO_3$ lattice, were all observed in the Raman spectrum of the thin film, suggesting the noncentrosymmetric nature of the film and thus the existence of a ferroelectric order.[11c,19] The strong Raman-active peaks at 138, 178, 550, and 780 cm^{-1} correspond to the transverse optical TO_1, TO_2, TO_4, and longitudinal optical LO_4 vibration modes (the inset in Figure 4a). Notably, the prominent TO_1 and TO_2 polar modes confirmed the emergence of spontaneous polarization in the thin film, which represented the off-center vibrations of Ti atoms and the relative vibration of Sr atoms toward TiO_6 octahedra, respectively.

Next, we considered the electronic origin of this interesting ferroelectric polarization. XAS can be utilized to reveal the bonding state and coordination environment for this ferroelectric polarization (Figure 4b). In an ideal TiO_6 octahedral configuration (O_h symmetry), similar to the case of cubic $SrTiO_3$, the five degenerate 3d-orbitals of Ti atoms split into triply degenerate low-energy t_{2g} orbitals and doubly degenerate high-energy e_g orbitals based on crystal field theory. When the TiO_6 octahedron is elongated along the c-axis and Ti is still at the center (D_{4h} symmetry), the degenerate orbitals further split with a decrease in the splitting energy (Δ) (Figure S9, Supporting Information).

The increased distance between Ti and O1 (hereinafter, the O atoms of the octahedron along the c-axis and the other four O atoms in the ab-plane are referred to as O1 and O2, respectively) results in a weakened hybridization and thus lowers the energy level of the e_g orbital from the O_h symmetry. However, because the off-center displacement of the Ti atom (C_{4v} symmetry) further triggers a stronger coupling of Ti $3d_{3z^2-r^2}$–O1 2p in the same orbital, the corresponding Ti 3d e_g peak intensity increases instead of decreasing as compared to the cause of TiO_6 with a D_{4h} symmetry (Figure 4b).[20] The off-center Ti atom relative to the ab-plane in the unit cell also weakens the Ti $3d_{x^2-y^2}$–O2 2p bonding, lowering the intensity of the t_{2g} peak. As shown in Figure 4b, the reduced energy difference between the t_{2g} and e_g peaks also verifies the reduction in Δ. In addition, the difference from 535 to 538 eV can be attributed to the Sr 4d–O 2p hybridization with the polar displacement of Sr atoms in the thin film.[20] Based on these facts, it can be concluded that the long-range order of ferroelectricity stabilized in the thin film originates from the intense Ti–O hybridization that counteracts the short-range repulsion.[21]

To further understand the origin of the tetragonal structure and strong ferroelectricity of the film, first-principles DFT calculations were conducted. We first calculated the Landau energy profile of the tetragonally strained film. During the calculation, the atomic positions were fully optimized, whereas the lattice constants were fixed to the experimental values (Table S2, Supporting Information). With the movement of Ti atoms along the c-axis, the total energy of the system features a classic

**ADVANCED
SCIENCE NEWS**

www.advancedsciencenews.com

**ADVANCED
MATERIALS**

www.advmat.de

double-well potential similar to that of perovskite-type ferroelectrics like $BaTiO_3$ and $PbTiO_3$ (Figure 4c).[21] Based on the Born effective charge approach, P_s in the unit cell was estimated to be 47.3 μC cm^{-2}. The disparity between the experimental and calculated values may be due to the fluctuating distribution of the c/a in the practical thin film and the temperature difference. Valence-electron density distribution and density of states in the tetragonal $SrTiO_3$ system demonstrated a stronger Ti 3d–O1 2p hybridization than that of Ti–O2 (Figure 4d; Figure S10, Supporting Information), which is consistent with the XAS results. Moreover, a slight hybridization between the off-center Sr atom and O2 atoms was noticed. From these calculated results, it can be inferred that the electronic structure and origins of the ferroelectricity in the strained tetragonal $SrTiO_3$ film are more similar to those in the case of the prototype $BaTiO_3$ than those in the case of $PbTiO_3$. We further studied the effects of different vacancies on the tetragonality of $SrTiO_3$ by DFT calculations (Figure 1d). It was found that charge-neutral Ti vacancy ($V_{Ti}^{\times}$) and O vacancy ($V_O^{\times}$) cannot induce a large c/a ratio by themselves. Interestingly, the combination of $V_{Ti}^{\times}$, $V_O^{\times}$, and additional electron doping (for example, due to other oxygen vacancies) can effectively lead to a large c/a ($\approx$1.036) and ferroelectric displacements (δ_{zTi} = 0.19 Å). This highlights the importance of Ti/O-deficient perovskite nanoregions for the emergence of ferroelectricity. These results are in good agreement with the experimental values and can also be verified by the simulated STEM images based on the theoretical model (Figure S11, Supporting Information). Therefore, our calculations are consistent with the experimental results and reveal the source of the coherent tensile strain and the nature of the polar tetragonal macrostructure.

3. Conclusion

Strong room-temperature ferroelectricity was achieved in strained $SrTiO_3$ homoepitaxial thin films by introducing electron-doped Ti/O-deficient perovskite nanoregions into the film. Through a purposeful modification of elemental stoichiometry, similar B/O-deficient nanoregions could also be generated in a range of paraelectric or ferroelectric ABO_3 perovskite compounds for controlling the strain state and improving performance. These nanoregions can induce a coherent lattice strain, either tensile or compressive, in the crystal lattice and thereby effectively tune the electronic structure for emergent physical properties. As opposed to that in traditional interfacial biaxial strain, strain relaxation will not occur with an increase in the thickness of the film. This study proposes a new paradigm for modulating functionalities in strongly correlated oxides, guiding the material design of robust ferroelectrics, high-temperature multiferroics, and superconductors.

4. Experimental Section

Target Synthesis and Thin Film Deposition: Both pure $SrTiO_3$ and Sr-rich ceramic targets were prepared by mixing $SrCO_3$ and TiO_2 powders through a conventional solid-state reaction in which the $SrCO_3$:TiO_2 molar ratios were maintained at 1:1 and 0.55:0.45, respectively. After complete ball-milling, both were sintered at

1573 K for 12 h. Thin films with a thickness of 260 nm were fabricated on (001)-oriented single-crystal $SrTiO_3$ substrates by the pulsed laser deposition. A KrF excimer laser with a wavelength of 248 nm was used to ablate the pure $SrTiO_3$ and Sr-rich targets at a repetition rate of 2 Hz and an energy density of 1.25 J cm^{-2} within a spot size of 4 × 6 mm^2 for depositing the normal and tetragonal $SrTiO_3$ thin films. During the deposition, the oxygen pressure and substrate temperature were controlled at 6 Pa and 1023 K, respectively. After deposition, the film was annealed in situ for 20 min under an oxygen pressure of 350 Pa, and then, the temperature was reduced to room temperature at a cooling rate of 5 K min^{-1}. For electric measurement, a fully strained $SrRuO_3$ bottom electrode with a thickness of 10 nm was first grown on the $SrTiO_3$ substrate using a commercial ceramic target before depositing the thin film.

Structural Characterization and Analysis: The macrostructure of the thin film was examined by synchrotron-based XRD at the X-ray diffuse scattering station (1W1A beamline) of the Beijing Synchrotron Radiation Facility and high-resolution diffractometer (PW3040/60, PANalytical, The Netherlands) with Cu Kα radiation. ABF-STEM images, HAADF-STEM images, and EDXS elemental maps were obtained on an aberration-corrected FEI Titan Themis G2 microscope operating at 300 kV. The collection angle for the HAADF and the ABF was 48–200 and 12–45 mrad, respectively. 2D EDXS elemental mapping for Sr and Ti was acquired on the Super-X EDXS system (4 quadrant SDD EDCS detector), which enables fast mapping with a high signal-collection efficiency. Accurate atomic positions in the STEM image were measured using the 2D Gaussian fitting, and the c/a ratio and polarization vector maps were calculated by the customized MATLAB scripts. Each HAADF image was acquired from different areas near the interface in the sample and then divided into two regions, namely, the thin film and the substrate for the integrated intensity calculations of the atomic columns and comparison. Integrated intensities of the Sr and Ti atomic columns in the image were normalized to the mean of the corresponding sublattice of the thin film and substrate, respectively, for the calculation of SD. The simulation of HAADF/ABF-STEM images was carried out using the Dr. Probe program.[22]

Electric Measurements: For ferroelectric loop measurements, the Pt dots, diameter = 100 μm, were deposited on the thin film as the top electrode by DC magnetron sputtering. Hysteresis loop measurements were performed using a ferroelectric analyzer (TF Analyzer 1000, aixACCT, Germany). Surface morphology and switching of ferroelectric domains were measured by PFM (MFP-3D, Asylum Research, USA, and Dimension Icon, Bruker, Germany). The temperature-dependent dielectric spectra were performed using Agilent E4980A (Agilent Technologies Company, Palo Alto, CA, USA).

XAS and Raman Spectroscopy Measurements: O K-edge X-ray absorption spectra were collected at the photoelectron spectroscopy station (4B9B beamline) of the Beijing Synchrotron Radiation Facility. Raman spectra of the thin film and substrate were measured using a Raman spectrometer (HR Evolution, Horiba, France) with a He–Cd excimer laser of 325 nm wavelength at the backscattering geometry.

DFT Calculations: The first-principles DFT calculations were carried out using the Vienna Ab initio Simulation Package (VASP).[23] The generalized gradient approximation (GGA) functional of the Perdew–Burke–Ernzerhof for solids (PBEsol) was used in order to obtain a more accurate lattice structure.[24] A 3 × 3 × 3 supercell containing 135 atoms was used in the calculation for the macrostructure of the tetragonal $SrTiO_3$ system. Then, one Ti atom and one O atom in the supercell were removed to simulate the distribution of Ti/O vacancies. The k-point mesh of 8 × 8 × 8 was used for integrations over the Brillouin zones of different cubic lattices of $SrTiO_3$. The tetrahedron method with Blöchl corrections was used to determine electronic states at each k point.[25] Electron wave functions were expanded with a plane wave basis up to cutoff energy of 500 eV, and all atoms were fully relaxed until the Hellmann–Feynman forces on them were less than 0.01 eV $Å^{-2}$. Electronic convergence was reached when the total energy differences were less than 1×10^{-5} eV. All DFT calculations were carried out at 0 K. The spontaneous polarizations of unit cells were

**ADVANCED
SCIENCE NEWS**

www.advancedsciencenews.com

**ADVANCED
MATERIALS**

www.advmat.de

calculated using the Born effective charge approach by the following equation

$$P_S = \frac{1}{V_u}\left(\frac{1}{8}Z_{Sr}^*\sum_{i=1}^{8}r_{Sr} + Z_{Ti}^*r_{Ti} + \frac{1}{2}Z_O^*\sum_{i=1}^{6}r_O\right) \qquad (1)$$

where V_u denotes the unit-cell volume, Z_{Sr}^*, Z_{Ti}^*, and Z_O^* represent the Born effective charges of Sr, Ti, and O atoms in the unit cell, respectively, which are obtained through density functional perturbation theory,[26] and r_{Sr}, r_{Ti}, and r_O denote the displacement of Sr, Ti, and O atoms from the initial positions in the normal $SrTiO_3$ unit cell, respectively.

Supporting Information

Supporting Information is available from the Wiley Online Library or from the author.

Acknowledgements

Conflict of Interest

The authors declare no conflict of interest.

Data Availability Statement

Research data are not shared.

Keywords

[1] a) J. F. Scott, C. A. Paz de Araujo, *Science* **1989**, *246*, 1400; b) J. F. Scott, *Science* **2007**, *315*, 954; c) R. Ramesh, *Thin Film Ferroelectric Materials and Devices*, Vol. *3*, Springer Science & Business Media, New York **2013**.

[2] a) N. Setter, D. Damjanovic, L. Eng, G. Fox, S. Gevorgian, S. Hong, A. Kingon, H. Kohlstedt, N. Y. Park, G. B. Stephenson, I. Stolitchnov, A. K. Tagantsev, D. V. Taylor, T. Yamada, S. Streiffer, *J. Appl. Phys.* **2006**, *100*, 051606; b) R. J. Zeches, M. D. Rossell, J. X. Zhang, A. J. Hatt, Q. He, C.-H. Yang, A. Kumar, C. H. Wang, A. Melville, C. Adamo, G. Sheng, Y.-H. Chu, J. F. Ihlefeld, R. Erni, C. Ederer, V. Gopalan, L. Q. Chen, D. G. Schlom, N. A. Spaldin, L. W. Martin, R. Ramesh, *Science* **2009**, *326*, 977; c) S. Zhang, F. Li, X. Jiang, J. Kim, J. Luo, X. Geng, *Prog. Mater. Sci.* **2015**, *68*, 1.

[3] a) T. Qi, I. Grinberg, A. M. Rappe, *Phys. Rev. B* **2010**, *82*, 134113; b) C.-H. Yang, D. Kan, I. Takeuchi, V. Nagarajan, J. Seidel, *Phys. Chem. Chem. Phys.* **2012**, *14*, 15953; c) J. M. Rondinelli, C. J. Fennie, *Adv. Mater.* **2012**, *24*, 1961; d) T. Shi, G. Li, J. Zhu, *Ceram. Int.* **2017**, *43*, 2910.

[4] a) J. Wang, J. B. Neaton, H. Zheng, V. Nagarajan, S. B. Ogale, B. Liu, D. Viehland, V. Vaithyanathan, D. G. Schlom, U. V. Waghmare, N. A. Spaldin, K. M. Rabe, M. Wuttig, R. Ramesh, *Science* **2003**, *299*, 1719; b) K. J. Choi, M. Biegalski, Y. L. Li, A. Sharan, J. Schubert, R. Uecker, P. Reiche, Y. B. Chen, X. Q. Pan, V. Gopalan, L.-Q. Chen, D. G. Schlom, C. B. Eom, *Science* **2004**, *306*, 1005; c) A. K. Yadav, C. T. Nelson, S. Hsu, Z. Hong, J. D. Clarkson, C. M. Schlepütz, A. R. Damodaran, P. Shafer, E. Arenholz, L. R. Dedon, D. Chen, A. Vishwanath, A. M. Minor, L. Q. Chen, J. F. Scott, L. W. Martin, R. Ramesh, *Nature* **2016**, *530*, 198; d) L. Zhang, J. Chen, L. Fan, O. Diéguez, J. Cao, Z. Pan, Y. Wang, J. Wang, M. Kim, S. Deng, J. Wang, H. Wang, J. Deng, R. Yu, J. F. Scott, X. Xing, *Science* **2018**, *361*, 494.

[5] K. M. Rabe, M. Dawber, C. Lichtensteiger, C. H. Ahn, J.-M. Triscone, in *Physics of Ferroelectrics: A Modern Perspective*, Vol. *105* (Eds: K. M. Rabe, C. H. Ahn, J.-M. Triscone), Springer-Verlag, Berlin, Germany **2007**, p. 1.

[6] a) S. Mueller, J. Mueller, A. Singh, S. Riedel, J. Sundqvist, U. Schroeder, T. Mikolajick, *Adv. Funct. Mater.* **2012**, *22*, 2412; b) M. Tyunina, J. Narkilahti, M. Plekh, R. Oja, R. M. Nieminen, A. Dejneka, V. Trepakov, *Phys. Rev. Lett.* **2010**, *104*, 227601; c) S. S. Rezaie, K. Ahadi, W. M. Strickland, S. Stemmer, *Phys. Rev. Lett.* **2020**, *125*, 087601; d) Y. F. Wei, P. Nukala, M. Salverda, S. Matzen, H. J. Zhao, J. Momand, A. S. Everhardt, G. Agnus, G. R. Blake, P. Lecoeur, J. Íñiguez, B. Dkhil, B. Noheda, *Nat. Mater.* **2018**, *17*, 1095.

[7] a) V. M. Goldschmidt, *Naturwissenschaften* **1926**, *14*, 477; b) V. M. Goldschmidt, T. Barth, G. Lunde, W. Zachriasen, *Skr. Nor. Vidensk.-Akad.* **1926**, *2*, 117; c) A. S. Bhalla, R. Guo, R. Roy, *Mater. Res. Innovations* **2000**, *4*, 3.

[8] a) K. A. Müller, H. Burkard, *Phys. Rev. B* **1979**, *19*, 3593; b) W. Zhong, D. Vanderbilt, *Phys. Rev. B* **1996**, *53*, 5047.

[9] M. Itoh, R. Wang, Y. Inaguma, T. Yamaguchi, Y. J. Shan, T. Nakamura, *Phys. Rev. Lett.* **1999**, *82*, 3540.

[10] J. H. Haeni, P. Irvin, W. Chang, R. Uecker, P. Reiche, Y. Li, S. Choudhury, W. Tian, M. E. Hawley, B. Craigo, A. K. Tagantsev, X. Q. Pan, S. K. Streiffer, L. Q. Chen, S. W. Kirchoefer, J. Levy, D. G. Schlom, *Nature* **2004**, *430*, 758.

[11] a) Y. S. Kim, D. J. Kim, T. H. Kim, T. W. Noh, J. S. Choi, B. H. Park, J.-G. Yoon, *Appl. Phys. Lett.* **2007**, *91*, 042908; b) H. W. Jang, A. Kumar, S. Denev, M. D. Biegalski, P. Maksymovych, C. W. Bark, C. T. Nelson, C. M. Folkman, S. H. Baek, N. Balke, C. M. Brooks, D. A. Tenne, D. G. Schlom, L. Q. Chen, X. Q. Pan, S. V. Kalinin, V. Gopalan, C. B. Eom, *Phys. Rev. Lett.* **2010**, *104*, 197601; c) D. Lee, H. Lu, Y. Gu, S.-Y. Choi, S.-D. Li, S. Ryu, T. Paudel, K. Song, E. Mikheev, S. Lee, S. Stemmer, D. A. Tenne, S. H. Oh, E. Y. Tsymbal, X. Wu, L. Q. Chen, A. Gruverman, C. B. Eom, *Science* **2015**, *349*, 1314.

[12] R. Xu, J. Huang, E. S. Barnard, S. S. Hong, P. Singh, E. K. Wong, T. Jansen, V. Harbola, J. Xiao, B. Y. Wang, S. Crossley, D. Lu, S. Liu, H. Y. Hwang, *Nat. Commun.* **2020**, *11*, 3141.

[13] a) S. A. Mabud, A. M. Glazer, *J. Appl. Crystallogr.* **1979**, *12*, 49; b) H. Evans, *Acta Crystallogr. B* **1961**, *14*, 1019.

[14] B. Jaffe, W. R. Cook, H. Jaffe, *Piezoelectric Ceramics*, Academic, London, UK **1971**.

[15] J. Wang, B. W. van Eerd, T. Sluka, C. Sandu, M. Cantoni, X. K. Wei, A. Kvasov, L. J. McGilly, P. Gemeiner, B. Dkhil, A. Tagantsev, J. Trodahl, N. Setter, *Nat. Mater.* **2015**, *14*, 985.

[16] a) B. Jaffe, *Piezoelectric Ceramics*, Vol. *3*, Elsevier, Amsterdam, The Netherlands **2012**; b) M. M. Kumar, V. R. Palkar, K. Srinivas, S. V. Suryanarayana, *Appl. Phys. Lett.* **2000**, *76*, 2764.

[17] a) T. Suzuki, Y. Nishi, M. Fujimoto, *Philos. Mag. A* **2000**, *80*, 621; b) T. Ohnishi, K. Shibuya, T. Yamamoto, M. Lippmaa, *J. Appl. Phys.* **2008**, *103*, 103703; c) C. M. Brooks, L. F. Kourkoutis, T. Heeg, J. Schubert, D. A. Muller, D. G. Schlom, *Appl. Phys. Lett.* **2009**, *94*, 162905.

[18] L. Jin, F. Li, S. J. Zhang, *J. Am. Ceram. Soc.* **2014**, *97*, 1.

[19] D. A. Tenne, A. K. Farrar, C. M. Brooks, T. Heeg, J. Schubert, H. W. Jang, C. W. Bark, C. M. Folkman, C. B. Eom, D. G. Schlom, *Appl. Phys. Lett.* **2010**, *97*, 142901.

[20] F. M. F. de Groot, J. Faber, J. J. M. Michiels, M. T. Czyżyk, M. Abbate, J. C. Fuggle, *Phys. Rev. B* **1993**, *48*, 2074.

[21] R. E. Cohen, *Nature* **1992**, *358*, 136.

[22] J. Barthel, *Ultramicroscopy* **2018**, *193*, 1.

[23] a) P. Hohenberg, W. Kohn, *Phys. Rev.* **1964**, *136*, B864; b) W. Kohn, L. J. Sham, *Phys. Rev.* **1965**, *140*, A1133; c) G. Kresse, J. Furthmüller, *Phys. Rev. B* **1996**, *54*, 11169; d) G. Kresse, D. Joubert, *Phys. Rev. B* **1999**, *59*, 1758.

[24] J. P. Perdew, A. Ruzsinszky, G. I. Csonka, O. A. Vydrov, G. E. Scuseria, L. A. Constantin, X. Zhou, K. Burke, *Phys. Rev. Lett.* **2008**, *100*, 136406.

[25] P. E. Blöchl, O. Jepsen, O. K. Andersen, *Phys. Rev. B* **1994**, *49*, 16223.

[26] a) R. King-Smith, D. Vanderbilt, *Phys. Rev. B* **1993**, *47*, 1651; b) R. Resta, *Rev. Mod. Phys.* **1994**, *66*, 899.